ACS APPLIED MATERIALS & INTERFACES

Research Article

www.acsami.org

Oxidation-Etching Preparation of MnO_2 Tubular Nanostructures for High-Performance Supercapacitors

Jixin Zhu,[†,‡] Wenhui Shi,[†] Ni Xiao,[†] Xianhong Rui,[†] Huiteng Tan,[†] Xuehong Lu,[†] Huey Hoon Hng,[†] Jan Ma,[†] and Qingyu Yan*[,†,‡]

[†]School of Materials Science and Engineering, Nanyang Technological University, Singapore 639798, Singapore

[‡]Energy Research Institute@NTU and TUM CREATE Research Centre@NTU, Nanyang Technological University, Singapore 637459, Singapore

Supporting Information

ABSTRACT: 1D hierarchical tubular MnO_2 nanostructures have been prepared through a facile hydrothermal method using carbon nanofibres (CNFs) as sacrificial template. The morphology of MnO_2 nanostructures can be adjusted by changing the reaction time or annealing process. Polycrystalline MnO_2 nanotubes are formed with a short reaction time (e.g., 10 min) while hierarchical tubular MnO_2 nanostructures composed of assembled nanosheets are obtained at longer reaction times (>45 min). The polycrystalline MnO_2 nanotubes can be further converted to porous nanobelts and sponge-like nanowires by annealing in air. Among all the types of MnO_2 nanostructures prepared, tubular MnO_2 nanostructures composed of assembled nanosheets show optimized charge storage performance when tested as supercapacitor electrodes, for example, delivering an power density of 13.33 $kW{\cdot}kg^{-1}$ and a energy density of 21.1 $Wh{\cdot}kg^{-1}$ with a long cycling life over 3000 cycles, which is mainly related to their features of large specific surface area and optimized charge transfer pathway.

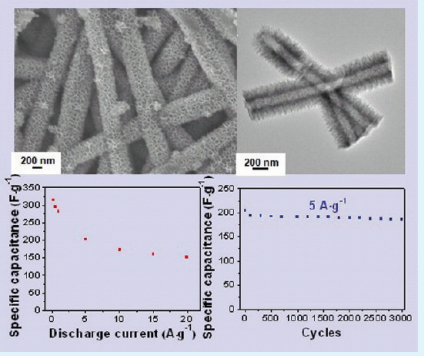

KEYWORDS: *MnO_2, carbon nanofibre, nanotubes, nanowires, nanobelts, supercapacitor*

INTRODUCTION

Supercapacitor, also known as electrochemical capacitor or ultracapacitor, has attracted growing interests because of its high power density, fast delivery rate and long cycle life, which plays an important role in complementing lithium-ion batteries in the energy storage field.[1,2] To achieve high energy storage performance, the exploration of novel electrode materials which generally have high surface area, high electrical conductivity, and involving redox-reactions is encouraged. Intensive research on the preparation of metal hydroxides, for example, $Co(OH)_2$,[3] $Ni(OH)_2$,[4] and metal oxides, such as MnO_2,[5−7] RuO_2,[8] Co_3O_4,[9] with various structures has been demonstrated to be potential candidates for supercapacitor. Furthermore, hybrid nanostructures, for example, metal oxide/graphene, have also been prepared to induce a synergetic contribution to improve their performance.[6,7,10−15]

As a promising candidate for supercapacitor electrode, MnO_2 has attracted great research interests because of its natural abundance, low cost and low toxicity.[6,7,11,16−18] Studies have indicated that the electrochemical performances of MnO_2 are largely dependent on their structure, size, and crystallinity.[18] The redox reactions are widely accepted as the major charge storage mechanism, which can be separated into (1) the surface adsorption of electrolyte cations, for example, Na^+, $(MnO_2)_{surface} + Na^+ + e^- \leftrightarrow (MnOONa)_{surface}$ and (2) the intercalation/deintercalation of electrolyte cations in the bulk, for example, $MnO_2 + Na^+ + e^- \leftrightarrow (MnOONa)$.[19] On the basis of such mechanism, 2D MnO_2 nanostructures, for example, nanoflakes or nanosheets, are expected to exhibit larger specific surface area and deliver better charge storage performance than their bulk counterparts. This is because such nanostructures can effectively combine the contribution from both surface- and bulk-redox reactions. However, one concern for the electrode formed from nanosheets or nanoflakes is that these 2D nanostructures may become electrically isolated due to the loose contacts between each other. On the other hand, 1D MnO_2 nanostructures,[5,16,17,20] which form 3D network-structured electrodes, may provide reliable electrical contract between the 1D structures as compared to that of isolated particles. Also, the hierarchical 1D nanostructures, for example, combination of nanotubes with ultrathin sheets, possess large surface area, which allows them to interact effectively with the Na^+ in the electrolyte and shorten the diffusion length of the charge carriers. There are much empty space in this 3D electrode, which can effectively buffer any volume change during charge/discharge.[21] Furthermore, the introduction of hollow channel inside the 1D nanostructures can enhance the

Received: March 2, 2012
Accepted: April 11, 2012
Published: April 11, 2012

effective interaction between the electrolyte and the electrode.[5,16,20]

Here, in this study, we prepared several different 1D MnO_2 nanostructures using a facile hydrothermal method coupled with rational post-treatments. When tested as supercapacitor electrodes, among all the 1D MnO_2 nanostructures, the hierarchical one formed by assembly of MnO_2 ultrathin sheets exhibited the best energy storage performance, for example, a high energy density of 21.1 $Wh{\cdot}kg^{-1}$ at a power density of 13.33 $kW{\cdot}kg^{-1}$.

EXPERIMENTAL SECTION

Carbon Nanofibers (CNFs) Preparation. Polyacrylonitrile (PAN, M_w = 150 000) dissolved in dimethylformamide (DMF) with 8 wt % was electrospun to obtain PAN nanofibers under 15 kV and 0.5 $mL{\cdot}h^{-1}$ for voltage and flow rate, respectively. The PAN nanofibers were dried at 60 °C in vacuum for 2 days and carbonized PAN nanofibers were obtained under the following conditions: heated from room temperature to 280 °C at a heating rate of 1 $°C{\cdot}min^{-1}$ in air, kept at 280 °C for 1 h; then heated from 280 to 550 °C at a heating rate of 10 $°C{\cdot}min^{-1}$ in argon environment, kept at 550 °C for 2.5 h; and finally cooled down to room temperature naturally.

MnO_2 Tube Structures. $KMnO_4$ (142 mg) was dissolved into 30 mL of deionized water by sonication and then carbon nanofibres with a size of 1 × 3 cm^2 were immersed into the solution. The mixture was sealed in a Teflon-lined autoclave and maintained at 160 °C for different reaction time, e.g. 10 minutes (named as MnO_2-10), 45 minutes (named as MnO_2-45), 180 minutes (named as MnO_2-180), and then taken out for cooling. After it was cooled down to room temperature, the precipitates were collected and washed using deionized water and ethanol. Among these samples, the MnO_2 tube structures prepared under 10 min were heated in deionized water at 100 °C for 30 min to remove the residual of $KMnO_4$.

Porous MnO_2 Nanobelts. The MnO_2-10 tube structures were heated in deionized water at 100 °C for 30 min and then dried. Finally, the samples were annealed at 500 °C for 10 min at a heating rate of 5 $°C{\cdot}min^{-1}$ to obtain porous belt-like MnO_2.

Sponge-like MnO_2 Nanowires. The MnO_2-10 tube structures were heated in 0.5 M glucose aqueous solution at 100 °C for 30 min and then dried. Finally, the samples were annealed at 500 °C for 10 min at a heating rate of 5 $°C{\cdot}min^{-1}$ to obtain porous belt-like MnO_2.

Characterizations. The morphology of the samples was investigated by using a field-emission scanning electron microscopy (FESEM) system (JEOL, Model JSM-7600F), and the nanostructures of the samples were characterized by using a transmission electron microscopy (TEM) system (JEOL, Model JEM-2100) operating at 200 kV. To investigate the samples using TEM, a suspension of the as-prepared sample, for example, MnO_2 in ethanol was drop-casted onto carbon-coated copper grids and dried under ambient condition. Crystal phases of the samples were identified using a Scintag PAD-V X-ray diffractometer with Cu Kα irradiation. Thermogravimetry analyses (TGA, Q500) was carried out in the temperature of 30 to 600 °C at a heating rate of 10 $°C{\cdot}min^{-1}$ in air. Nitrogen adsorption/desorption isotherms were measured on a Micromeritics TriStar 3000 porosimeter (mesoporous characterization) and Micromeritics ASAP 2020 (microporous characterization) at 77 K. All samples were outgassed at 100 °C for 6 h under vacuum before measurements were recorded. The specific surface areas were calculated using the Brunauer–Emmett–Teller (BET) method.

Electrochemical Measurements. To fabricate film electrodes, 80 wt % active material (e.g., MnO_2), 10 wt % acetylene black, and 10 wt % polyvinylidene fluoride (PVDF) binder were mixed into *N*-methyl-2-pyrrolidinone (NMP). The obtained slurry was coated onto 2 × 1 cm^2 graphite papers within an area of 1 × 1 cm^2, which were then dried in vacuum at 50 °C for 12 h to remove the solvent. The electrochemical properties and capacitance measurements of the supercapacitor electrodes were studied in a three-electrode half-cell system in 1 M Na_2SO_4 electrolyte with Solartron analytical equipment (Model 1470E). Platinum wire was used as the counter electrode and Ag/AgCl as the reference electrode. Platinum wire was used as a counter electrode and Ag/AgCl as the reference electrode. Electrochemical impedance spectroscopy (EIS) measurements were carried out in the frequency range from 10 kHz to 0.1 Hz at open circuit potential with an ac perturbation of 10 mV with the help of an impedance spectrum analyzer (Solatron, SI 1255B Impedance/gain-phase analyzer; computer software ZView).

RESULTS AND DISCUSSION

The preparation of MnO_2 tubular nanostructures was achieved through the reaction of $KMnO_4$ with CNFs via a hydrothermal route. In the process, $KMnO_4$ is reduced to MnO_2 and deposited on the surface of CNFs, while CNFs are oxidized to CO_2 simultaneously. The CO_2 is released to form CO_3^{2-} in the solution and the MnO_2 nanosheets are further grown on the predeposited MnO_2 tubes with increased reaction times to form the MnO_2 tubular nanostructures. The CNFs used as templates in this synthesis show diameters of ~200 nm and lengths up to hundreds of micrometers (Supporting Information Figure S1).

The crystal structure of the samples prepared with different reaction times was examined using X-ray diffraction patterns (XRD). The XRD patterns (Figure 1) confirm the formation of

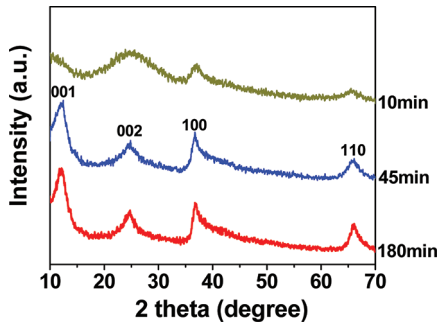

Figure 1. X-ray diffraction patterns (XRD) of MnO_2 obtained under different reaction time: 10, 45, and 180 min.

birnessite MnO_2 (JCPDS 43-1456) with no other crystalline phase. An obvious broadening of the peak width is observed for MnO_2 obtained after 10-min reaction, which is mainly related to poor crystallinity. On the basis of the full width at high maximum of (002) peak of MnO_2-45 and MnO_2-180, the crystalline domain size along [002] is estimated to be only ~2.4 and 2.6 nm, respectively using Scherrer's equation. Compared to sample MnO_2-10, the samples of MnO_2-45 and MnO_2-180 exposed large (001) facets that XRD patterns depict a strong (001) peak.

The morphologies of the oxide samples prepared with different reaction times are depicted in Figure 2. After 10 min reaction (MnO_2-10), the tubular samples (Figure 2a and b), with a diameter of ~200 nm, duplicate the original shape of the CNFs templates. The TEM image indicates that the wall thickness of the MnO_2 tubes is 25–45 nm. There are nanopores (Supporting Information Figure S2) in the wall of these MnO_2-10 samples, which are possibly generated due to the release of CO_2 during the oxidation of CNFs. The HRTEM observation (Figure 2c) reveals that these MnO_2 tubes are polycrystalline. The observed lattice fringes with a distance of 0.31 nm corresponds to the (002) planes of birnessite MnO_2 (JCPDS43-1456). Increasing the reaction time to 45 min (MnO_2-45) leads to the growth of tubular MnO_2 with a diameter of ~350 nm (Figure 2d and e). The wall thickness of

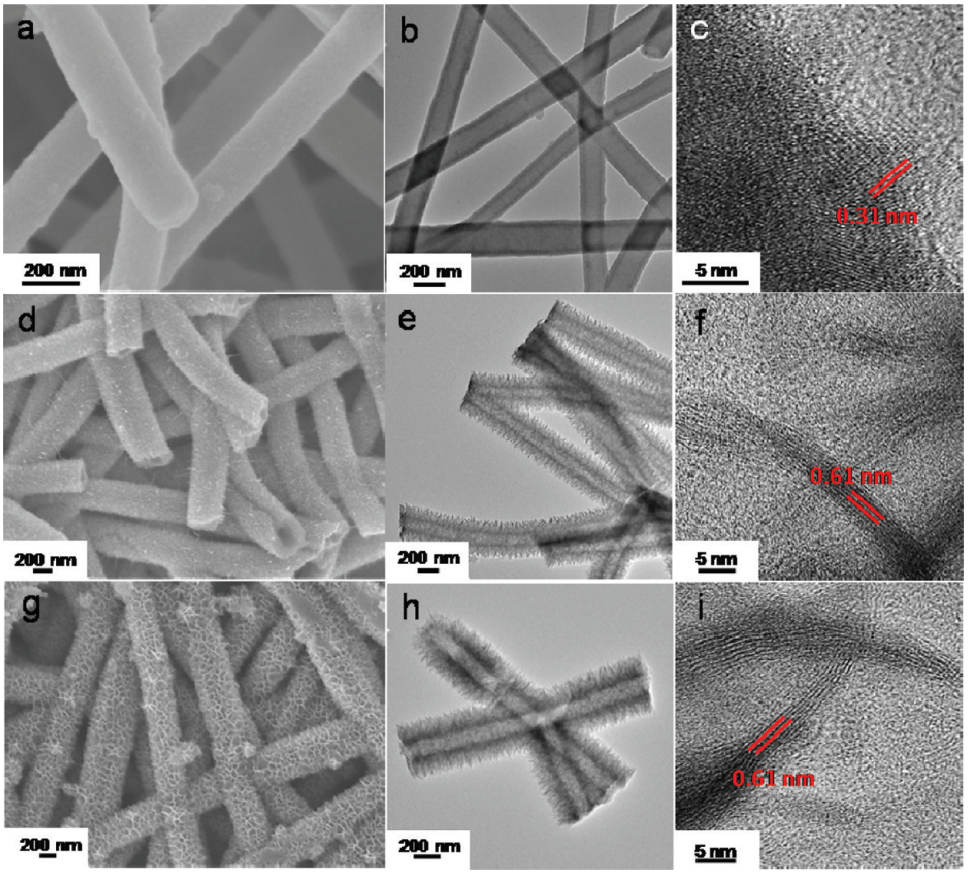

Figure 2. FESEM and TEM images of MnO_2 tube nanostructures obtained under different reaction time (a–c) 10 min. (d–f) 45 min, and (g–i) 180 min.

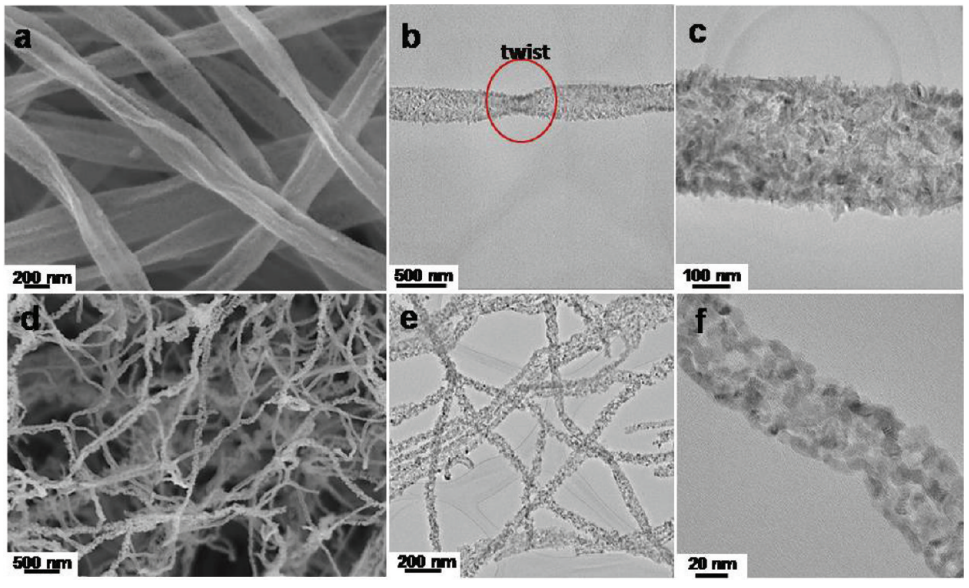

Figure 3. FESEM and TEM images of (a–c) porous MnO_2 nanobelts prepared by washing MnO_2-10 in DI water and then annealed at 500 °C for 10 min at a heating rate of 5 °C·min^{-1} in Air; circle in b indicates a twist of nanobelts; (d–f) sponge-like MnO_2 nanowires prepared by washing MnO_2-10 in glucose aqueous solution and then annealed at 500 °C for 10 min at a heating rate of 5 °C·min^{-1} in air.

these MnO_2-45 samples (e.g., ~100 nm) is much larger than that of MnO_2-10 tubes due to the seeded growth of MnO_2 nanosheets on the walls of MnO_2 tubes. The tubular MnO_2-45 samples are mostly open ended as indicated from the TEM images (Figure 2e) and the hollow interior can be examined directly from the cross-section image (Supporting Information Figure S3). The HRTEM image displays clear lattice fringes of 0.61 nm, which corresponds to the interplane spacing of (001) planes of birnessite type MnO_2 (Figure 2f).[22] By increasing the reaction time further to 180 min (MnO_2-180), the resulting

dx.doi.org/10.1021/am300388u | ACS Appl. Mater. Interfaces 2012, 4, 2769–2774

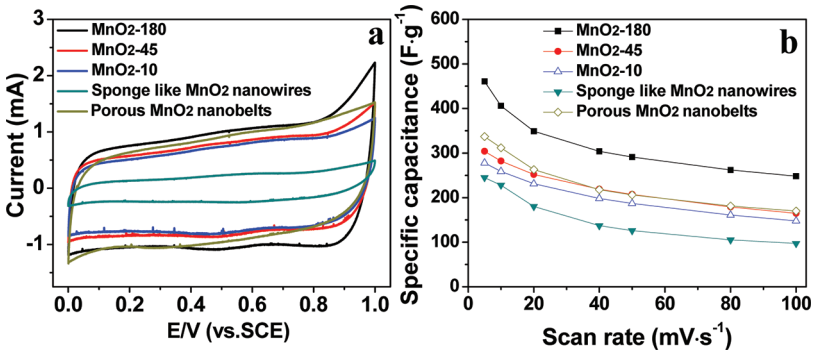

Figure 4. (a) Representative cyclic voltammetry (CV) curves of MnO_2-10, MnO_2-45, MnO_2-180, porous MnO_2 nanobelts and sponge-like MnO_2 nanowires at a scan rate of 5 mV·s^{-1}; (b) comparison of specific capacitances of MnO_2-10, MnO_2-45, MnO_2-180, porous MnO_2 nanobelts and sponge-like MnO_2 nanowires at different scan rates.

samples show obvious layered-structure feature grown on the wall of the tubes (Figure 2g). These sheets are highly transparent to electron beams under TEM, indicating ultrathin thicknesses (Figure 2h). The diameter of the tube further increases to ~470 nm and the wall thickness of these MnO_2-180 samples is around ~180 nm. The HRTEM image of these MnO_2 nanosheets shows typical lengths of ~140 nm and widths of 3−5 nm (Figure 2i). Thermal gravimetric analysis (TGA) was used to examine the content of the residual CNFs templates in the composites of MnO_2-10, MnO_2-45, and MnO_2-180 (Supporting Information Figure S4). The calculated weight percentage of MnO_2 in MnO_2-10, MnO_2-45, and MnO_2-180 are 84.3%, 92.8%, and 93.5%. Here, the weight loss in the range of 23−150 °C is attributed to water loss.

The MnO_2-10 sample can be further processed to form different 1D nanostructures after rational treatments. Porous nanobelts (Figure 3a−c) are formed after refluxing the MnO_2-10 nanostructures in deionized water under 100 °C for 30 min and annealing the samples at 500 °C for 10 min. Here, the washing process is to remove the additional unreacted Mn precursor. The XRD pattern (Supporting Information Figure S5) confirms that the porous nanobelts are birnessite MnO_2. The nanobelts are possibly formed due to the shrinkage of the tubes, where the walls are folded together. It is evidenced from the widths of these MnO_2 nanobelts (e.g., ~500 nm) which are much larger than the diameter of the original MnO_2-10 tubes. The porous nanobelts with thicknesses of ~70−100 nm are twisted and consisted of many small nanoparticles (Figure 3b and c).

Interestingly, sponge-like nanowires are formed after washing the MnO_2-10 tube samples in 0.5 M glucose aqueous solution at 100 °C for 30 min and then dried and annealing the sample at 500 °C for 10 min (Figure 4d−e). The XRD pattern (Supporting Information Figure S5) confirms that the porous sponge-like nanowires are also birnessite MnO_2. The sponge-like MnO_2 nanowires show smaller diameters, for example, 40−65 nm (Figure 4d−f), as compared to that of the nanobelts. The sponge-like nanowires are composed of loosely connected small nanoparticles. Here, during the immersion process, the glucose molecules can be absorbed into MnO_2-10 tubes after dry, which was converted to carbon and then burned into CO_2 during the annealing process. At the starting stage, the formation of carbon can maintain the wire shape of MnO_2 without structural collapse and then the formed carbon was changed into CO_2 with increasing temperature in Air. This leads to the generation of structural cracks or raptures of the original nanotubes. High concentration of glucose will lead to the formation of smaller piece of MnO_2 due to structural collapse, which is due to the large amount of CO_2 and heat energy released during the annealing process.

These 1D MnO_2 nanostructures were tested as supercapacitor electrodes by using cyclic voltammetry (CV) over a range of scan rates of 5−100 mV·s^{-1} and galvanostatic charge/discharge measurements over a current of 0.2−20 A·g^{-1} within the potential range of 0.0−1.0 V in 1 M Na_2SO_4 aqueous solution with a three-electrode system (Supporting Information Figure S6 and Supporting Information Figure S7). Representative CVs at a scan rate of 5 mV/s show small peaks at around 0.5 and 0.85 V for all the sample electrodes (Supporting Information Figure S8), for example, MnO_2-10, MnO_2-45, MnO_2-180, porous nanobelts and sponge-like nanowires, which indicates that the redox reactions are taking place during the charge/discharge process (Figure 4a). The specific capacitances of the MnO_2 electrodes (Figure 4b) are calculated from the CVs according to the equation: $C = Q/\Delta Vm$, where C (F·g^{-1}) is the specific capacitance, m(g) is the mass of the active material in the working electrode, Q(C) is the average charge during the charging and discharging process, and ΔV (V) is the potential window. It reveals that the MnO_2-180 electrode depicts high specific capacitances of 461 F·g^{-1} and 248 F·g^{-1} at scan rates of 5 mV·s^{-1} and 100 mV·s^{-1}, respectively. In comparison, the other electrodes show lower specific capacitance. For example, the porous MnO_2 nanobelts show specific capacitances of 337 and 170 F·g^{-1} at scan rates of 5 and 100 mV·s^{-1}, while the sponge-like MnO_2 nanowires depict capacitances of 245 and 97 F·g^{-1} at scan rates of 5 and 100 mV·s^{-1}.

The specific capacitances of the electrode can also be estimated from the discharge curves according to the equation: $C = I\Delta t/\Delta Vm$, where I is the constant discharging current and Δt is the discharging time. The results (Figure 5a) show that the MnO_2-180 electrode depicts a high specific capacitance of 315 F·g^{-1} at a current of 0.2 A·g^{-1}. The specific capacitance decreases to 152 F·g^{-1} when the current density increases to 20 A·g^{-1}. Such energy storage performance is promising as compared to some reported values on MnO_2 based electrodes, for example, composites, or MnO_2/graphene hybrids.[6,17,23−26] On the basis of the galvanostatic charge/discharge results, the energy density (E) and power density (P) of the MnO_2 tubes electrode can be calculated from the following equations: $E = 1/2C(\Delta V)^2$ and $P = E/t$. Among all the electrodes tested, the MnO_2-180 electrode exhibits the highest energy density of 21.1

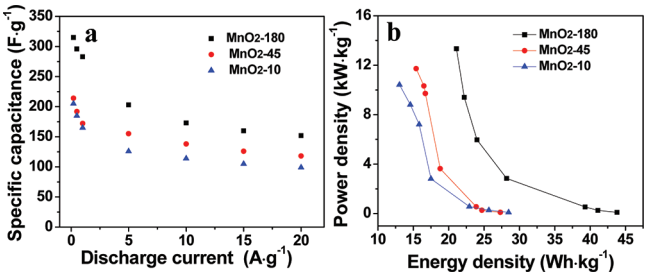

Figure 5. (a) Comparison of specific capacitances between MnO_2-180, MnO_2-45, and MnO_2-10 tubes at different currents; (b) comparison of energy densities and power densities between MnO_2-180, MnO_2-45, and MnO_2-10 tubes.

$Wh{\cdot}kg^{-1}$ at a maximum power density of 13.33 $kW{\cdot}k^{-1}$. The better electrochemical energy storage performance of the MnO_2-180 electrode is mainly attributed to its structural features, e.g. the larger specific surface area (~90 $m^2{\cdot}g^{-1}$, Supporting Information Figure S9), well crystallized grains and interconnected 1D tubular nanostructures, which allow the electrolyte to effectively interact with the active materials and shorten the diffusion paths of the charge carriers. Electrochemical impedance spectroscopy was used to evaluate of the kinetic and mechanistic information of MnO_2-10, MnO_2-45, and MnO_2-180 electrode materials (Supporting Information Figure S10). The inclined portion of the curve (about 45°) in the middle frequency is ascribed to the Warburg, which indicates good ion diffusion/transport in the electrolyte to the electrode surface.[12,27] The cycling stability of MnO_2-180 electrode was investigated at a current density of 5 $A{\cdot}g^{-1}$ over 3000 cycles (Figure 6). With the first-cycle capacitance of

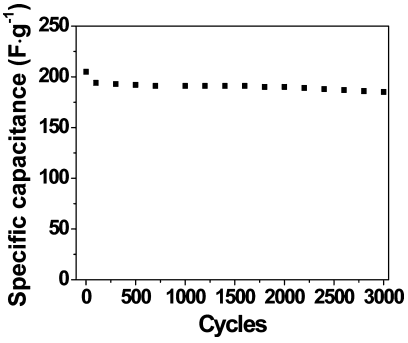

Figure 6. Cycling performance of MnO_2-180 tubes at a current density of 5 $A{\cdot}g^{-1}$ in 1 M Na_2SO_4 aqueous solution.

205 $F{\cdot}g^{-1}$, the MnO_2-180 electrode delivers a capacitance of 185 $F{\cdot}g^{-1}$ during the 3000th cycle. The capacitive retention is about 99.99% per cycle, indicating excellent cyclability.

In summary, various MnO_2 1D hierarchical nanostructures are prepared through a facile hydrothermal method. MnO_2 tubular structures are obtained by using CNFs as sacrificial template and the morphologies of MnO_2 can be changed by adjusting the reaction time and post-treatment. Evaluated as electrode for supercapacitor, the MnO_2 tubular structures consisting of ultrathin nanosheets (MnO_2-180) are found to demonstrate superior charge storage performance with good capacitance retention, for example, an energy density of 13.33 $kW{\cdot}kg^{-1}$ at a power density of 21.1 $Wh{\cdot}kg^{-1}$.

CONCLUSIONS

In summary, various MnO_2 1D hierarchical nanostructures are prepared through a facile hydrothermal method. MnO_2 tubular structures are obtained by using CNFs as sacrificial template and the morphologies of MnO_2 can be changed by adjusting the reaction time and post-treatment. Evaluated as electrode for supercapacitor, the MnO_2 tubular structures consisting of ultrathin nanosheets (MnO_2-180) are found to demonstrate superior charge storage performance with good capacitance retention, e.g. an energy density of 13.33 $kW{\cdot}kg^{-1}$ at a power density of 21.1 $Wh{\cdot}kg^{-1}$.

ASSOCIATED CONTENT

Supporting Information

Additional figures are described in the text. This information is available free of charge via the Internet at http://pubs.acs.org/.

AUTHOR INFORMATION

Corresponding Author

*E-mail: alexyan@ntu.edu.sg. Tel: +65 6790 4583. Fax: +65 6790 9081.

Notes

The authors declare no competing financial interest.

ACKNOWLEDGMENTS

The authors gratefully acknowledge AcRF Tier 1 RG 31/08 of MOE (Singapore), NRF2009EWT-CERP001-026 (Singapore), Singapore Ministry of Education (MOE2010-T2-1-017), A*STAR SERC grant 1021700144 and Singapore MPA 23/04.15.03 RDP 009/10/102 and MPA 23/04.15.03 RDP 020/10/113 grant.

REFERENCES

(1) Arico, A. S.; Bruce, P.; Scrosati, B.; Tarascon, J.-M.; van Schalkwijk, W. *Nat. Mater.* **2005**, *4*, 366−377.
(2) Simon, P.; Gogotsi, Y. *Nat. Mater.* **2008**, *7*, 845−854.
(3) Chang, J. K.; Wu, C. M.; Sun, I. W. *J. Mater. Chem.* **2010**, *20*, 3729−3735.
(4) Guan, C.; Liu, J. P.; Cheng, C. W.; Li, H. X.; Li, X. L.; Zhou, W. W.; Zhang, H.; Fan, H. *J. Energy Environ. Sci.* **2011**, *4*, 4496−4499.
(5) Yan, W. B.; Ayvazian, T.; Kim, J. Y.; Liu, Y.; Donavan, K. C.; Xing, W. D.; Yang, Y. A.; Hemminger, J. C.; Penner, R. M. *ACS Nano* **2011**, *5*, 8275−8287.
(6) Chen, S.; Zhu, J. W.; Wu, X. D.; Han, Q. F.; Wang, X. *ACS Nano* **2010**, *4*, 2822−2830.
(7) Wu, Z. S.; Ren, W. C.; Wang, D. W.; Li, F.; Liu, B.; Cheng, H. M. *ACS Nano* **2010**, *4*, 5835−5842.
(8) Hu, C. C.; Chang, K. H.; Lin, M. C.; Wu, Y. T. *Nano Lett.* **2006**, *6*, 2690−2695.
(9) Xia, X. H.; Tu, J. P.; Mai, Y. J.; Wang, X. L.; Gu, C. D.; Zhao, X. B. *J. Mater. Chem.* **2011**, *21*, 9319−9325.
(10) Liu, R.; Duay, J.; Lee, S. B. *Chem. Commun.* **2011**, *47*, 1384−1404.
(11) He, Y. B.; Li, G. R.; Wang, Z. L.; Su, C. Y.; Tong, Y. X. *Energy Environ. Sci.* **2011**, *4*, 1288−1292.
(12) Shi, W. H.; Zhu, J. X.; Sim, D. H.; Tay, Y. Y.; Lu, Z. Y.; Zhang, X. J.; Sharma, Y.; Srinivasan, M.; Zhang, H.; Hng, H. H.; Yan, Q. Y. *J. Mater. Chem.* **2011**, *21*, 3422−3427.
(13) Zhu, J. X.; Zhu, T.; Zhou, X. Z.; Zhang, Y. Y.; Lou, X. W.; Chen, X. D.; Zhang, H.; Hng, H. H.; Yan, Q. Y. *Nanoscale* **2011**, *3*, 1084−1089.
(14) Zhu, J. X.; Lu, Z. Y.; Oo, M. O.; Hng, H. H.; Ma, J.; Zhang, H.; Yan, Q. Y. *J. Mater. Chem.* **2011**, *21*, 12770−12776.
(15) Zhu, J. X.; Yin, Z. Y.; Li, H.; Tan, H. T.; Chow, C. L.; Zhang, H.; Hng, H. H.; Ma, J.; Yan, Q. Y. *Small* **2011**, *7*, 3458−3464.

(16) Dong, S. M.; Chen, X.; Gu, L.; Zhou, X. H.; Li, L. F.; Liu, Z. H.; Han, P. X.; Xu, H. X.; Yao, J. H.; Wang, H. B.; Zhang, X. Y.; Shang, C. Q.; Cui, G. L.; Chen, L. Q. *Energ. Environ. Sci.* **2011**, *4*, 3502−3508.
(17) Jiang, H.; Zhao, T.; Ma, J.; Yan, C. Y.; Li, C. Z. *Chem. Commun.* **2011**, *47*, 1264−1266.
(18) Devaraj, S.; Munichandraiah, N. *J. Phys. Chem. C* **2008**, *112*, 4406−4417.
(19) Wei, W. F.; Cui, X. W.; Chen, W. X.; Ivey, D. G. *Chem. Soc. Rev.* **2011**, *40*, 1697−1721.
(20) Kim, J.-H.; Lee, K. H.; Overzet, L. J.; Lee, G. S. *Nano Lett.* **2011**, *11*, 2611−2617.
(21) Lee, S. W.; Gallant, B. M.; Byon, H. R.; Hammond, P. T.; Yang, S. H. *Energy Environ. Sci.* **2011**, *4*, 1972−1985.
(22) Liu, J. P.; Jiang, J.; Cheng, C. W.; Li, H. X.; Zhang, J. X.; Gong, H.; Fan, H. J. *Adv. Mater.* **2011**, *23*, 2076−2081.
(23) Roberts, A. J.; Slade, R. C. T. *Energ. Environ. Sci.* **2011**, *4*, 2813−2817.
(24) Lei, Z. B.; Zhang, J. T.; Zhao, X. S. *J. Mater. Chem.* **2011**, *22*, 153−160.
(25) Zhang, J. T.; Jiang, J. W.; Zhao, X. S. *The J. Phys. Chem. C* **2011**, *115*, 6448−6454.
(26) Yu, G. H.; Hu, L. B.; Vosgueritchian, M.; Wang, H. L.; Xie, X.; McDonough, J. R.; Cui, X.; Cui, Y.; Bao, Z. N. *Nano Lett.* **2011**, *11*, 2905−2911.
(27) Zhu, J. X.; Sharma, Y. K.; Zeng, Z. Y.; Zhang, X. J.; Srinivasan, M.; Mhaisalkar, S.; Zhang, H.; Hng, H. H.; Yan, Q. Y. *J. Phys. Chem. C* **2011**, *115*, 8400−8406.